Article

Long-range interactions driving neighboring Fe–N$_4$ sites in Fenton-like reactions for sustainable water decontamination

Zelin Wu[1,2,5], Zhaokun Xiong[1,2,5], Bingkun Huang[1,2], Gang Yao[2,3], Sihui Zhan [4] ✉ & Bo Lai [1,2] ✉

Actualizing efficient and sustainable environmental catalysis is essential in global water pollution control. The single-atom Fenton-like process, as a promising technique, suffers from reducing potential environmental impacts of single-atom catalysts (SACs) synthesis and modulating functionalized species beyond the first coordination shell. Herein, we devised a high-performance SAC possessing impressive Fenton-like reactivity and extended stability by constructing abundant intrinsic topological defects within carbon planes anchored with Fe–N$_4$ sites. Coupling atomic Fe–N$_4$ moieties and adjacent intrinsic defects provides potent synergistic interaction. Density functional theory calculations reveal that the intrinsic defects optimize the d-band electronic structure of neighboring Fe centers through long-range interactions, consequently boosting the intrinsic activity of Fe–N$_4$ sites. Life cycle assessment and long-term steady operation at the device level indicate promising industrial-scale treatment capability for actual wastewater. This work emphasizes the feasibility of synergistic defect engineering for refining single-atom Fenton-like chemistry and inspires rational materials design toward sustainable environmental remediation.

Developing highly efficient and durable heterogeneous catalysts is crucial for remediating growing water contamination[1–3]. In recent decades, single-atom catalysts (SACs) have been extensively explored for basic research and practical applications in peroxymonosulfate (PMS)-based advanced oxidation processes (AOPs) owing to numerous unique properties[4–6]. SACs based on diverse metal centers and supports have been designed and employed for PMS activation to generate reactive oxygen species (ROS)[7,8]. SACs for industrial catalytic applications are expected to possess excellent catalytic performance coupled with long-term operation lifetime. The intense interaction between reactive metal centers and reaction intermediate products renders metal sites of SACs easily occupied and deactivated, leading to

declines in catalytic stability[9,10]. Moreover, although SACs can maximize the utilization of metal atoms to reduce metal consumption, the synthesis involves cumbersome and complex processes. The high production costs associated with expensive precursors or supports (e.g., metal-organic frameworks (MOFs) and MXene) and high energy consumption, as well as the potential environmental impact of toxic chemicals, contravene the environmental concept of sustainable development[11,12]. Thus, developing SACs with high activity in a green and economical manner persists in pivotal challenges to extend to real-world applications.

Carbon-based Fe SACs equipped with Fe–N–C moieties are favored by researchers due to the merits of high reactivity, low

[1]State Key Laboratory of Hydraulics and Mountain River Engineering, College of Architecture and Environment, Sichuan University, Chengdu, China. [2]Sino-German Centre for Water and Health Research, Sichuan University, Chengdu, China. [3]Sino-German Centre for innovative Environmental Technologies (WATCH E.V.), Aachen, Germany. [4]Key Laboratory of Pollution Processes and Environmental Criteria (Ministry of Education), College of Environmental Science and Engineering, Nankai University, Tianjin, China. [5]These authors contributed equally: Zelin Wu, Zhaokun Xiong. ✉e-mail: sihuizhan@nankai.edu.cn; laibo@scu.edu.cn

toxicity, and environmental friendliness[13,14]. Further upgrading the intrinsic activity of SACs and understanding molecular-scale reaction mechanisms are current spotlights, and most efforts are devoted to unfolding the catalytic potential of single-atom sites by tuning metal center and local structures in the first coordination shell (FCS)[15–17]. Typically, regulating configurations, coordination numbers, and coordinated-atom types in FCS are effective ways to manipulate the properties of SACs. However, although FCS directly bonded to metal atoms intensely governs SACs, studies have rarely focused on long-range structural components beyond FCS. Owing to multiple underlying non-metallic functionalized species (e.g., functional groups, heteroatom doping sites, and intrinsic carbon defects) that generally exist in carbon supports of carbon-based SACs, it is urgent to maneuver these long-range species precisely and interpret modulating effects on electronic structures and activity.

Intrinsic topological defects contribute significantly to the properties of carbon nanomaterials, enhancing the performance of critical catalytic reactions[18–20]. Concerning carbon-based SACs, defects probably alter charge and energy distributions of neighboring metal−N−C (M−N−C) sites and create abundant reactant-accessible active sites to potentiate the transfer of substrates and electrons, thus accelerating reaction kinetics[21–25]. In contrast, current reported SACs-based systems ignore the underlying contributions of intrinsic carbon defects, which are prevalent in carbon-based catalysts prepared by pyrolysis. Unfortunately, the high vacancy-formation energy in pristine graphene suggests enormous difficulties involving removing lattice carbon atoms[26]. Alternatively, eliminating external N atoms by thermal treatment permits readier access to vacancies in graphene, inducing the formation of topological defects[27]. However, before elucidating modulation mechanisms of intrinsic defects on M−N−C sites, a significant challenge is preserving the original FCS configurations of M−N−C sites intact following the construction of intrinsic defects. Regulating pyrolysis temperatures to produce intrinsic carbon defects may be accompanied by alterations in FCS microenvironments in M−N−C sites, such as transitions from M−N₄ to M−N₃ and M−N₂ or introducing M−C coordination[28,29]. Hence, the controllable construction of microscopic defects in SACs without disturbing local FCS configurations of M−N−C sites is crucial for unraveling the synergistic optimization of overlooked defect engineering in SACs.

Herein, we design a superior Fenton-like catalyst by constructing abundant intrinsic defects within carbon planes anchored with Fe−N₄ sites (D−FeN₄−C). Low-cost sources and eco-friendly assembly strategy induce N elimination to create intrinsic defects without shifting the FCS coordination environments of Fe−N₄ sites. Coupling intrinsic defects and Fe−N₄ sites performed robust synergistic effects and significantly strengthened PMS activation. Density functional theory (DFT) calculations demonstrate that long-range interactions from intrinsic defects on neighboring Fe−N₄ sites elevate the intrinsic reactivity of Fe−N₄ sites and promote reactive FeN₄=O generation. Furthermore, intrinsic defects can function as cleaner for adjacent Fe−N₄ sites to realize long-term stability and environmental sustainability. This study provided promising perspectives for optimizing the intrinsic reactivity and revealing the structure-activity relationship of SACs by synergistic topological carbon defects.

Results

Fabrication of intrinsic carbon defects in Fe SAC
A facile thermal treating strategy based on temperature-dependent N elimination was developed for controlled constructions of intrinsic defects without altering FCS coordination structures of Fe−N−C sites, as illustrated in Fig. 1a. C-riched Fe-doped g-C₃N₄ was selected as precursors derived from thermal condensations of dicyandiamide (DCD) and 1-(2-cyanoethyl)-2-phenylimidazole (CEPI) molecules incorporated with trace amounts of Fe salts. CEPI contributed to the formation of C-riched Fe-g-C₃N₄, providing additional carbon sources

during carbonation and improving the defect levels and the yields of products (Supplementary Figs. 1, 2). Further carbonized at higher pyrolysis temperatures to eliminate partial N atoms, and C atoms are involved in the rearrangement, creating substantial topological defects in carbon products anchored with isolated Fe−N₄ sites to yield D−FeN₄−C[30]. In contrast, relatively low-temperature thermal treatments obtained FeN₄−C with low-defect levels, and corresponding metal-free samples were fabricated without adding Fe salts (defect-rich sample denoted as D−NC, low-defect sample denoted as NC) (Supplementary Fig. 3).

High-angle annular dark-field (HAADF) and aberration-corrected HAADF scanning transmission electron microscopy (AC-HAADF-STEM) images reveal Fe species evenly doped in carbon matrixes in both FeN₄−C and D−FeN₄−C, evidencing atomic dispersion of Fe species (Fig. 1b–d,f–h). The relevant elemental mapping diagrams (Supplementary Fig. 4) show that C, N, and Fe elements are uniformly distributed. Besides, the atom-overlapping Gaussian-function-fitting results from AC-HAADF-STEM displayed additional spatial information concerning the atomically dispersed Fe centers (Fig. 1e, i). X-ray diffraction (XRD) patterns of samples present only two broad peaks at 25.2° and 43.6°, correlating to the graphitized (002) and (101) planes, respectively, lacking Fe nanostructures or clusters (Supplementary Fig. 5). According to inductively coupled plasma optical emission spectrometry (ICP-OES) measurements, the mass loading of Fe was 0.72 wt% in FeN₄−C and 0.69 wt% in D−FeN₄−C (Supplementary Fig. 6).

No significant Fe 2p peak can be detected in X-ray photoelectron spectroscopy (XPS) due to the ultralow contents (Supplementary Fig. 7). High-resolution N 1s XPS spectra in Fig. 1j show that the dopant N atoms were eliminated more effectively as pyrolysis temperatures elevated (from FeN₄−C to D−FeN₄−C). The N signal intensity of D−FeN₄−C is much weaker than that of FeN₄−C, and the total N content reduces from 17.7% to 7.9%, suggesting substantial intrinsic carbon defects may be created by N atoms removal in D−FeN₄−C. In C 1s spectra (Fig. 1k), the proportion of sp^3 energy levels assigned to defective sp^3 carbon atoms increased in D−FeN₄−C, and the sp^2/sp^3 ratio dropped from 3.7 to 2.8 relative to FeN₄−C, signifying more carbon defects in D−FeN₄−C[24,31]. Structural variations are verified by Raman spectroscopy with the intensity of the D band sensitive to in-plane structural imperfection increased significantly as treatment temperatures increased (Fig. 1l), and the D band to G band intensity ratio (I_D/I_G) also elevated in D−FeN₄−C[31]. Electron paramagnetic resonance (EPR) (Fig. 1m and Supplementary Fig. 8) further evaluated the defect levels and the substantially higher EPR signal intensities at g = 2.004 of defective samples (D−FeN₄−C and D−NC) than those of FeN₄−C and NC, demonstrating the high-concentrations topological defects[23]. Combined with the micro/mesoporous pore size distribution in Brunauer-Emmett-Teller (BET) analysis and the intact carbon planes of D−FeN₄−C showed in atomic force microscope (AFM) images, indicated the limited holes and edge defects (Supplementary Figs. 9, 10). AC-TEM images showed direct evidence for the dominance of topological carbon defects created by eliminating several N atoms in the D−FeN₄−C (Supplementary Fig. 11). These results collectively confirmed that removing N atoms by thermal treatment for fabricating intrinsic topological defects is practicable.

Atomic structure and chemical state analysis of Fe SACs
To reveal the local electronic structures and chemical coordination environments of FeN₄−C and D−FeN₄−C at atomic scales, X-ray absorption spectroscopy (XAS) was performed. The Fe K-edge X-ray absorption near-edge structure (XANES) spectra show that the energies of FeN₄−C and D−FeN₄−C are situated between Fe foil and Fe₂O₃ and almost overlap with Fe phthalocyanine (FePc) (Fig. 2a), implying partial oxidation states of Fe species. As for the Fourier-transformed extended X-ray absorption fine structure (FT-EXAFS) spectra of FeN₄−C and D−FeN₄−C, only a prominent peak located at 1.45 Å
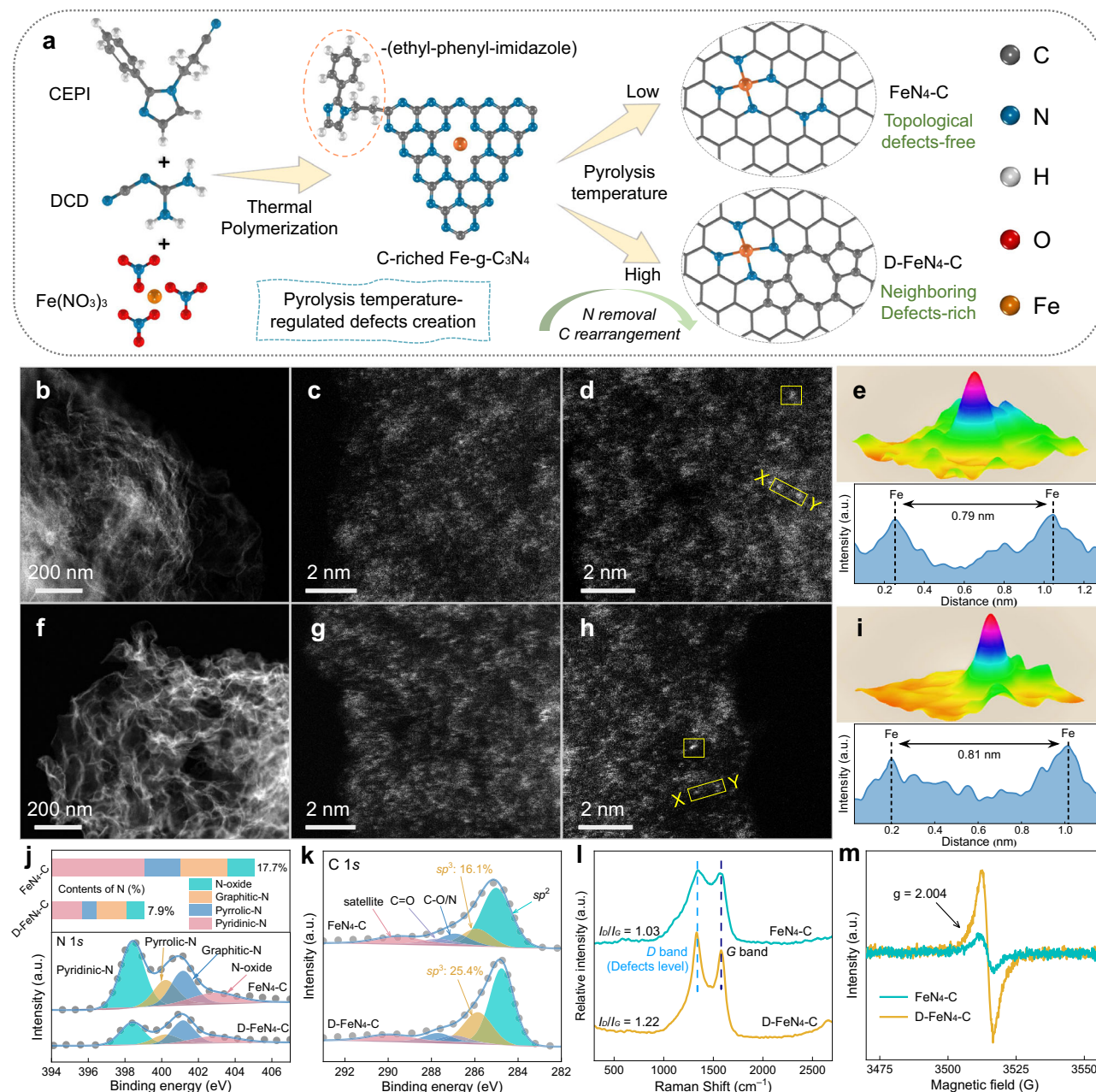
Fig. 1 | Synthetic scheme and structural properties of as-fabricated SACs. **a** Schematic illustration of the synthetic procedure of catalysts. **b**–**d** HAADF and AC-HAADF-STEM images of FeN₄–C. **e** Atom-overlapping Gaussian-function-fitting mapping of the square and intensity profile along X-Y in **d**. **f**–**h** HAADF and AC-HAADF-STEM images of D–FeN₄–C. **i** Atom-overlapping Gaussian-function-fitting mapping of the square and intensity profile along X-Y in **h**. **j** Distribution of N species and high-resolution N 1s XPS spectra, **k** C 1s XPS spectra, **l** Raman spectra, and **m** EPR spectra of FeN₄–C and D–FeN₄–C. Source data are provided as a Source Data file.

assigned to Fe−N scattering paths is observed for FeN₄−C and D−FeN₄−C (Fig. 2b), and no Fe−Fe interaction peak emerges at 2.15 Å, confirms the atomically dispersed Fe species[23]. Further EXAFS fitting analysis on k-space and R-space yielded quantitative structural parameters surrounding central Fe atoms, Fe−N₄ configuration is verified in both FeN₄−C and D−FeN₄−C (Fig. 2c, d; Supplementary Figs. 12, 13 and Supplementary Table 1). EXAFS wavelet transforms (WT) show that a clear WT intensity maximum is observed only at 4.1 Å⁻¹ for FeN₄−C and D−FeN₄−C, ascribed to the Fe−N coordination and perfectly coincides with FePc (Fig. 2e), in line with the above results[13].

⁵⁷Fe Mössbauer spectra measurements were conducted to analyze the components of Fe species in FeN₄−C and D−FeN₄−C. The Mössbauer spectrum for both FeN₄−C and D−FeN₄−C could be

deconvoluted into doublet and no singlet and sextet, excluding the existence of zero-valence Fe phases, in accordance with XAS and AC-HAADF-STEM results (Fig. 2f, g). All the curves can be fitted with two components, assigned to doublet 1 (D1, high-spin Feᴵᴵᴵ−N₄ species) and doublet 2 (D2, high-spin Feᴵᴵ−N₄ species), respectively (fitting parameters are listed in Supplementary Table 2)[32,33]. Quantitative analyses reveal that the high-spin Feᴵᴵᴵ−N₄ species was the dominant component in D−FeN₄−C with a relative content of 72.7%, much higher than that of FeN₄−C (57.6%). Simultaneously, the specific ratio of the two contents (D1/D2) in D−FeN₄−C was elevated to 2.66 than FeN₄−C of 1.36 (Fig. 2h). The above results indicated that the construction of neighboring intrinsic carbon defects modified the distribution of Fe species and resulted in more conversion of Fe−N₄ sites to high-spin Feᴵᴵᴵ−N₄ species
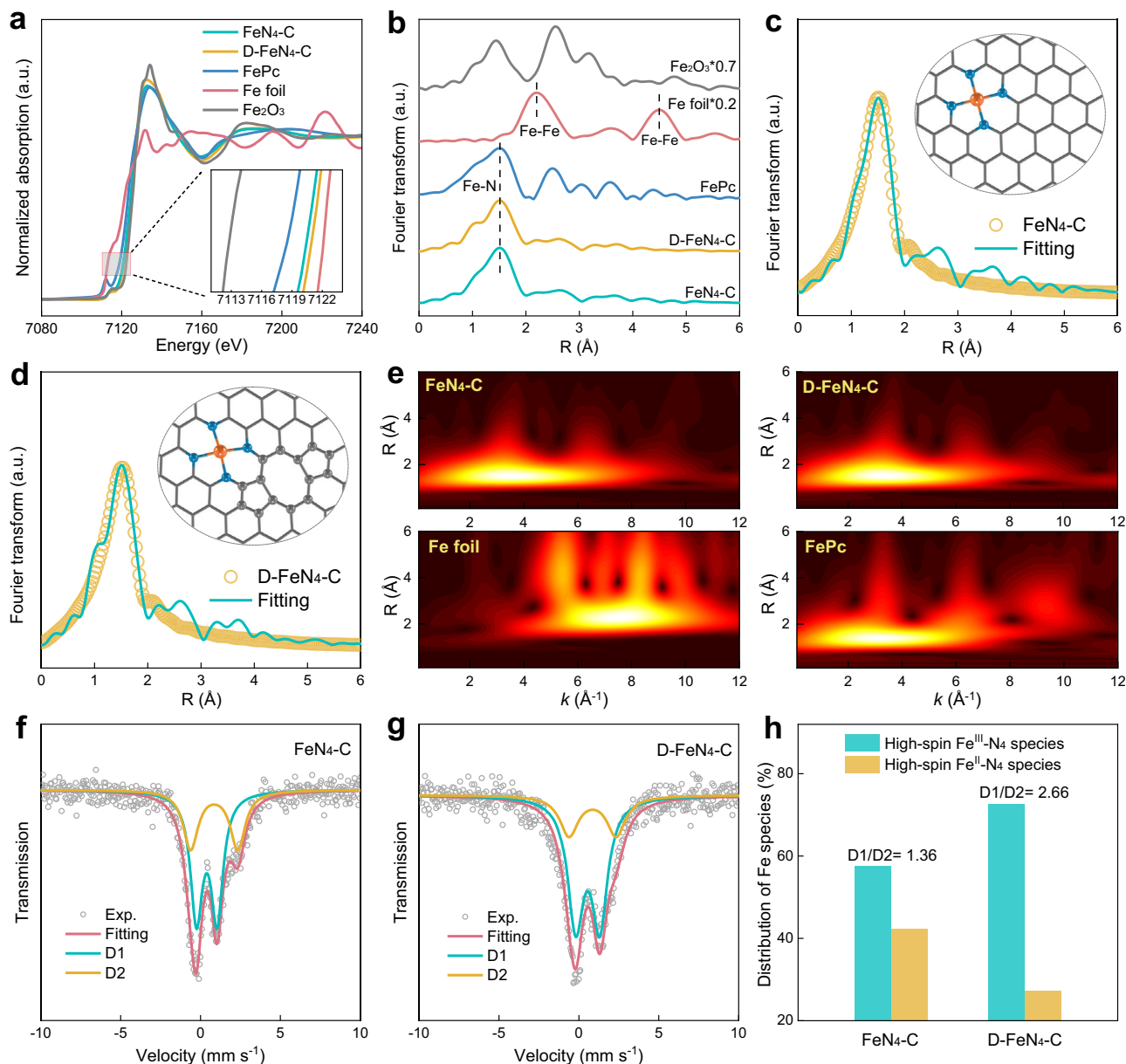
Fig. 2 | Atomic structural analysis of as-fabricated SACs. a XANES (inset: magnification of local areas) and **b** FT-EXAFS spectra in R-space of FeN$_4$–C, D–FeN$_4$–C and reference samples at Fe K-edge. **c, d** Corresponding FT-EXAFS fitting of Fe K-edge in R-space of FeN$_4$–C and D–FeN$_4$–C (inset: theoretical model structures). **e** WT spectra of Fe K-edge EXAFS for samples. **f, g** ^{57}Fe Mössbauer spectra of FeN$_4$–C and D–FeN$_4$–C. **h** Different Fe species distribution in FeN$_4$–C and D–FeN$_4$–C. Source data are provided as a Source Data file.

in D–FeN$_4$–C. Coupling with the XAS results and Mössbauer spectra analysis, atomically dispersed Fe species with different components extend throughout the carbon planes of FeN$_4$–C and D–FeN$_4$–C. Essentially, the homogeneity of the carbon substrate properties (except for intrinsic defects) and the FCS coordination structures for FeN$_4$–C and D–FeN$_4$–C are confirmed. All the above findings permit reasonable attempts to attribute the catalytic behavioral differences to the primary parametric variable of intrinsic defects.

Evaluation of Fenton-like reactivity

The Fenton-like reaction activity of the catalysts was evaluated through PMS activation to eliminate sulfisoxazole (SIZ), a typical antibiotic contaminant. Although adsorption alone could remove about 20% of SIZ, it has negligible effects on the high-speed catalytic degradation with incorporated PMS (Supplementary Fig. 14). Considerable oxygen-containing groups (C=O and C–O–C) and N-doped

sites in NC and high-concentration intrinsic defects in D–NC as potential reactive sites failed to efficiently activate PMS suffered from the lack of reactive Fe–N$_4$ sites (Fig. 3a). The catalytic activity of FeN$_4$–C significantly enhanced after introducing isolated Fe–N$_4$ sites and the observed rate constants (k_{obs}) increased by 4.2-fold compared with referential NC (Fig. 3b). The poisoning tests conducted by potassium thiocyanate (KSCN) further support that Fe–N$_4$ sites serve as authentic active sites for FeN$_4$–C and D–FeN$_4$–C (Supplementary Fig. 15). Concurrently, the k_{obs} for D–FeN$_4$–C demonstrated a tremendous 9.3-fold improvement over corresponding non-metallic defective D–NC. Notably, D–FeN$_4$–C carrying both intrinsic defects and Fe–N$_4$ sites exhibited remarkable efficiency with the k_{obs} as high as 0.548 min^{-1}, which is 3.1-fold superior to that of FeN$_4$–C (0.178 min^{-1}). These results suggest intense associations between the abundant intrinsic defects and atomic Fe–N$_4$ sites, and modifying intrinsic defects enhanced the reactivity of Fe–N$_4$ sites.
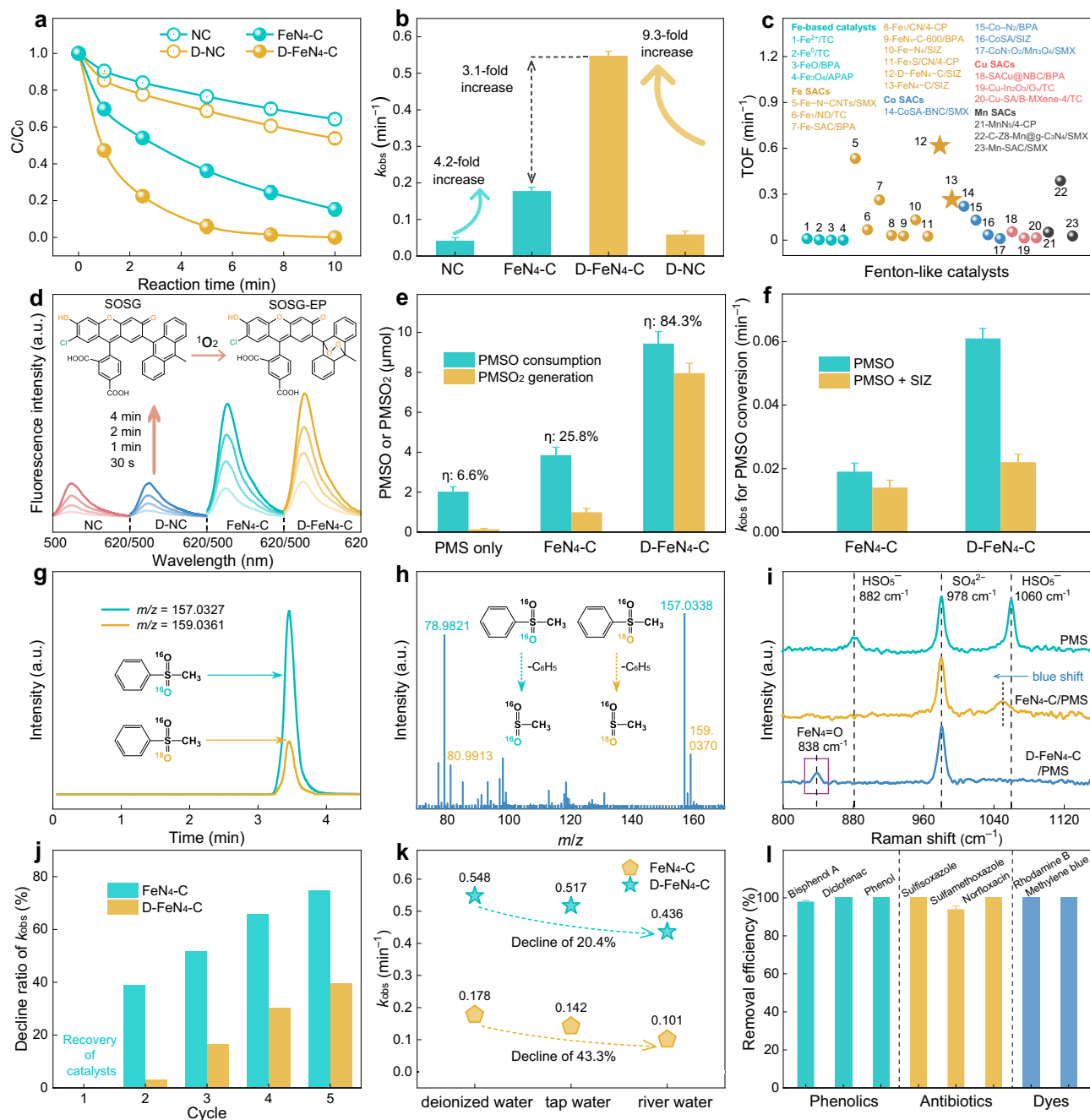
Fig. 3 | Fenton-like catalytic performance, reactive intermediates identification and environmental applicability analysis. a SIZ degradation in different systems. **b** Comparison of kinetics of catalytic systems. **c** Comparison of TOF values with state-of-the-art Fenton-like catalysts. **d** Time-dependent fluorescence intensity obtained from $^1O_2$ captured by SOSG. **e** PMSO consumption and $PMSO_2$ generation in catalytic systems. **f** Influence of SIZ on PMSO conversion. **g** Extracted ion chromatography of $PMS^{16}O^{16}O$ and $PMS^{16}O^{18}O$ generated from $PMS^{16}O$ in the D−FeN₄−C/ PMS system in $H_2^{18}O$. **h** MS^2 spectrum of $PMS^{16}O^{16}O$ and $PMS^{16}O^{18}O$. **i** In situ Raman spectra. **j** Decline ratio of k_{obs} in reusability tests for SIZ removal. **k** The k_{obs} of reaction systems under different water substrates. **l** Removal ratio of multiple model pollutants in the D−FeN₄−C/PMS system. Reaction condition: $[pollutant]_0 = 20\ \mu M$, $[PMS]_0 = 0.2\ mM$, $[catalyst] = 0.05\ g\ L^{-1}$, $[TBA] = [MeOH] = [FFA] = [Carotene] = 0.1–500\ mM$ (if any), initial pH = 6.5. Error bars are standard error values of three tests ($n = 3$). Source data are provided as a Source Data file.

It is worth noting that although higher-temperature pyrolysis contributed to removing more N species and producing more intrinsic defects, the agglomeration of Fe species renders the inferior reactivity to atomic FeN₄-C and D−FeN₄-C (Supplementary Fig. 16). D−FeN₄−C possesses the lowest N content and also contains identical oxygen-containing groups as FeN₄−C but exhibits the best reactivity, suggesting that the reactivity is primarily governed by defects level rather than other non-metallic functional species in carbon substrates. The turnover frequency (TOF) was employed to quantitatively evaluate the

intrinsic reactivity versus previously reported Fenton-like catalysts. Figure 3c and Supplementary Table 3 show that D−FeN₄−C exhibits excellent normalized intrinsic reactivity compared to the reported Fe-based catalysts and state-of-the-art SACs, as evidenced by a high TOF efficiency ($0.62\ min^{-1}$).

Identification of reactive species in Fenton-like reactions

The introduction of intrinsic defects can potentially impact catalytic reaction behaviors of Fe−N₄ sites. Chemical quenching experiments

were conducted to identify the prevailing ROS generated within these systems. Weak inhibition on SIZ degradation by tert-butanol (TBA), methanol (MeOH), and p-benzoquinone (p-BQ) as quenchers of radicals and signal-free EPR trapping imply negligible contributions of radicals (Supplementary Fig. 17)[34]. In contrast, furfuryl alcohol (FFA) and carotene significantly suppressed SIZ removal in the FeN$_4$−C/PMS system, confirming the dominant role of $^1O_2$, yet the contributions of $^1O_2$ in the D−FeN$_4$−C/PMS system evidently weakened. For further probe $^1O_2$, EPR tests show that introducing Fe−N$_4$ sites considerably boosts the $^1O_2$ generation and signal intensities recorded in FeN$_4$−C/PMS and D−FeN$_4$−C/PMS systems proved equivalent (Supplementary Figs. 18, 19). Highly supported by Singlet Oxygen Sensor Green (SOSG) probe tests, with strengthened $^1O_2$ generation induced by Fe−N$_4$ sites and consistent $^1O_2$ intensities in both systems (Fig. 3d)[17]. The lifetime of $^1O_2$ in D$_2$O (~68 µs) far exceeds that in H$_2$O (~3.7 µs)[35], and the kinetically accelerated oxidation in FeN$_4$−C/PMS is higher than D−FeN$_4$−C/PMS after transferring the $^1O_2$-based systems into D$_2$O (Supplementary Fig. 20). Collectively, it is speculated that creating substantial intrinsic defects in D−FeN$_4$−C strengthens other nonradical mechanisms beyond $^1O_2$ (electron transfer mechanisms or high-valent metal-oxo species).

Electron transfer pathways may be involved in multi-phase catalytic oxidation, especially for carbon materials[36]. Involving the pre-mixing of catalyst and PMS, SIZ degradation in catalytic systems is inhibited as the extended pre-mixing time (Supplementary Fig. 21). Combined with the depletion of PMS (Supplementary Fig. 22), PMS interacts with Fe−N$_4$ sites, thus decomposed and continuously consumed in catalytic processes, and this behavior deviates from the characteristics of electron transfer mechanisms. Open circuit voltage tests further recorded the voltage variation in catalytic systems (Supplementary Fig. 23), and PMS injection resulted in an elevated potential at the surface of the catalyst-coated electrode. However, the subsequent addition of SIZ triggered no discernible voltage jump. The above results demonstrate the absence of electron transfer mechanisms in principal mechanisms for SIZ elimination in FeN$_4$−C/PMS and D−FeN$_4$−C/PMS systems.

Upon the above exclusion, it is reasonable to assume that the enhanced catalytic performance of D−FeN$_4$−C stems from the contribution of high-valent FeN$_4$=O species. Chemical probing of methyl phenyl sulfoxide (PMSO) was performed to identify FeN$_4$=O species by selectively oxidizing PMSO to generate methyl phenyl sulfone (PMSO$_2$) via oxygen atoms transfer (OAT)[35,37,38]. PMS alone cannot oxidize PMSO to produce PMSO$_2$, and FeN$_4$−C/PMS converted limited PMSO with a yield (ηΔPMSO$_2$/ΔPMSO) of only 25.8% (Fig. 3e and Supplementary Fig. 24). As anticipated, considerable conversion of PMSO and high concentrations of PMSO$_2$ were detected in the D−FeN$_4$−C/PMS system. The ηΔPMSO$_2$/ΔPMSO representing the selectivity of OAT reaction reached 84.3%, suggesting the crucial role of high-valent FeN$_4$=O. Consequently, PMSO oxidization was significantly suppressed by adding competing SIZ to the PMSO conversion system (Fig. 3f and Supplementary Fig. 25), indicating that the FeN$_4$=O intermediates are highly reactive to SIZ, highlighting the essential contribution of high-valent FeN$_4$=O in SIZ removal. The Fe−O bond in FeN$_4$=O can exchange O atoms with solvent water, so ^{18}O isotopically labeled PMSO$_2$ (C$_7$H$_8$^{16}O^{18}O) was also determined. When the reaction system transferred to the H$_2$^{18}O matrix, two peaks with m/z = 157.0327 and m/z = 159.0361 were detected (Fig. 3g), ascribed to PMS^{16}O^{16}O and PMS^{16}O^{18}O, suggesting that ^{18}O isotope occurs OAT reaction among H$_2$^{18}O, FeN$_4$=O and PMS^{16}O^{16}O. Furthermore, a deviation of two mass units was observed in characteristic segments of PMSO$_2$, demonstrating the presence of FeN$_4$=O species (Fig. 3h).

In situ Raman was performed to observe the surface interactions during PMS activation (Fig. 3i). The PMS solution showed characteristic peaks of HSO$_5^-$ at 882/1060 cm^{-1} and SO$_4^{2-}$ at 978 cm^{-1}. After adding FeN$_4$−C, the characteristic peaks attributed to HSO$_5^-$ almost disappeared, indicating the rapid decomposition of PMS upon contact with the catalyst. A blueshift of the residual peak was also observed, suggesting that the chemical adsorption process transferred electrons from the catalyst to PMS and formed a few adsorption complexes. However, beyond the fast decomposition of PMS observed during the coupling of D−FeN$_4$−C to PMS, a new peak at 838 cm^{-1} representing the surface-active Fe species (high-valent FeN$_4$=O) was also identified[37,39]. Meanwhile, high-valent FeN$_4$=O oxidized amino and aromatic rings and induced SIZ degradation, as abundant OAT products were found during SIZ degradation, consistent with the analysis of reaction mechanisms (Supplementary Fig. 26 and Supplementary Table 4). These results demonstrate that intrinsic defects strengthened the formation of FeN$_4$=O species as complementary ROS with $^1O_2$ catalyzed by D−FeN$_4$−C.

Environmental applicability analysis

Subsequently, the catalytic stability of Fe SACs was studied. D−FeN$_4$−C exhibits superior reusability with a slight decline in reactivity after five cycles and maintained complete SIZ removal within 10 min (Supplementary Fig. 27). In contrast, the recycling performance of FeN$_4$−C is relatively inferior, with k_{obs} declining by 74.7% in the fifth cycle, whereas D−FeN$_4$−C dropped by only 39.6% (Fig. 3j). Pyridinic-N species distribution before and after reactions of D−FeN$_4$−C varied less than that of FeN$_4$−C, moderating the poisoning effects induced by the occupation of the pyridinic-N-coordinated Fe−N$_4$ sites by intermediates (Supplementary Fig. 28). Moreover, the reduction of intrinsic defect levels during cycling is responsible for the progressive inactivation of D−FeN$_4$−C (Supplementary Fig. 29). Interestingly, the catalytic reactivity of D−FeN$_4$−C could recover entirely after regeneration associated with the reconstructed pyridinic-N species and defect levels by thermal treatment (Supplementary Figs. 30, 31). Accordingly, the proportion of Fe leaching from reaction systems in cycling is minimal and consistent under 25 µg L^{-1}, far below the limit of 300 µg L^{-1} in standards for drinking water quality of China (GB 5749-2022) (Supplementary Fig. 32)[39]. Simultaneously, the catalytic systems were highly resistant to coexisting anions and organic compounds, and D−FeN$_4$−C sustained high reactivity in tap and river water matrices with only 20.4% loss in k_{obs} compared with 43.3% decreases in FeN$_4$−C (Fig. 3k, see Supplementary Figs. 33, 34 with accompanying detailed discussion, parameters are listed in Supplementary Table 5), implying that intrinsic defects endow D−FeN$_4$−C with superior stability and practicability. The D−FeN$_4$−C/PMS system can also selectively oxidize multiple electron-donating model pollutants efficiently with various molecular structures and chemical properties, including phenols, antibiotics and dye-based substances, demonstrating the broad environmental applicability (Fig. 3l and Supplementary Fig. 35).

Mechanisms of defects-induced long-range interactions

DFT calculations were carried out to understand the critical role of intrinsic defects and the formation mechanism of high-valent FeN$_4$=O species. Considering the intrinsic topological defects dominate in D−FeN$_4$−C from characterizations, the 585-type topological defect structure (two five-membered rings sandwiching an eight-membered ring) rearranged from optimizing V2 configuration (vacancies missing two carbon atoms) was constructed neighboring the Fe−N$_4$ site (Supplementary Fig. 36)[26,27,40]. Creating adjacent intrinsic defects at Fe−N$_4$ sites significantly promotes PMS adsorption according to adsorption energy (E_{ads}) calculations (Supplementary Fig. 37). Simultaneously, modifying topological defects converted from V1 and V3 vacancies via C-atom rearrangements shows consistent behavioral patterns of activity enhancement on adjacent Fe−N$_4$ sites (Supplementary Fig. 38). Furthermore, the role of intrinsic defects and oxygen-containing groups as potential active sites deserves to be explored[41,42]. As evidenced by E_{ads} calculations, PMS adsorption capacities of the 585 defects and oxygen-containing groups (C−O−C and C=O) (−1.56 eV to
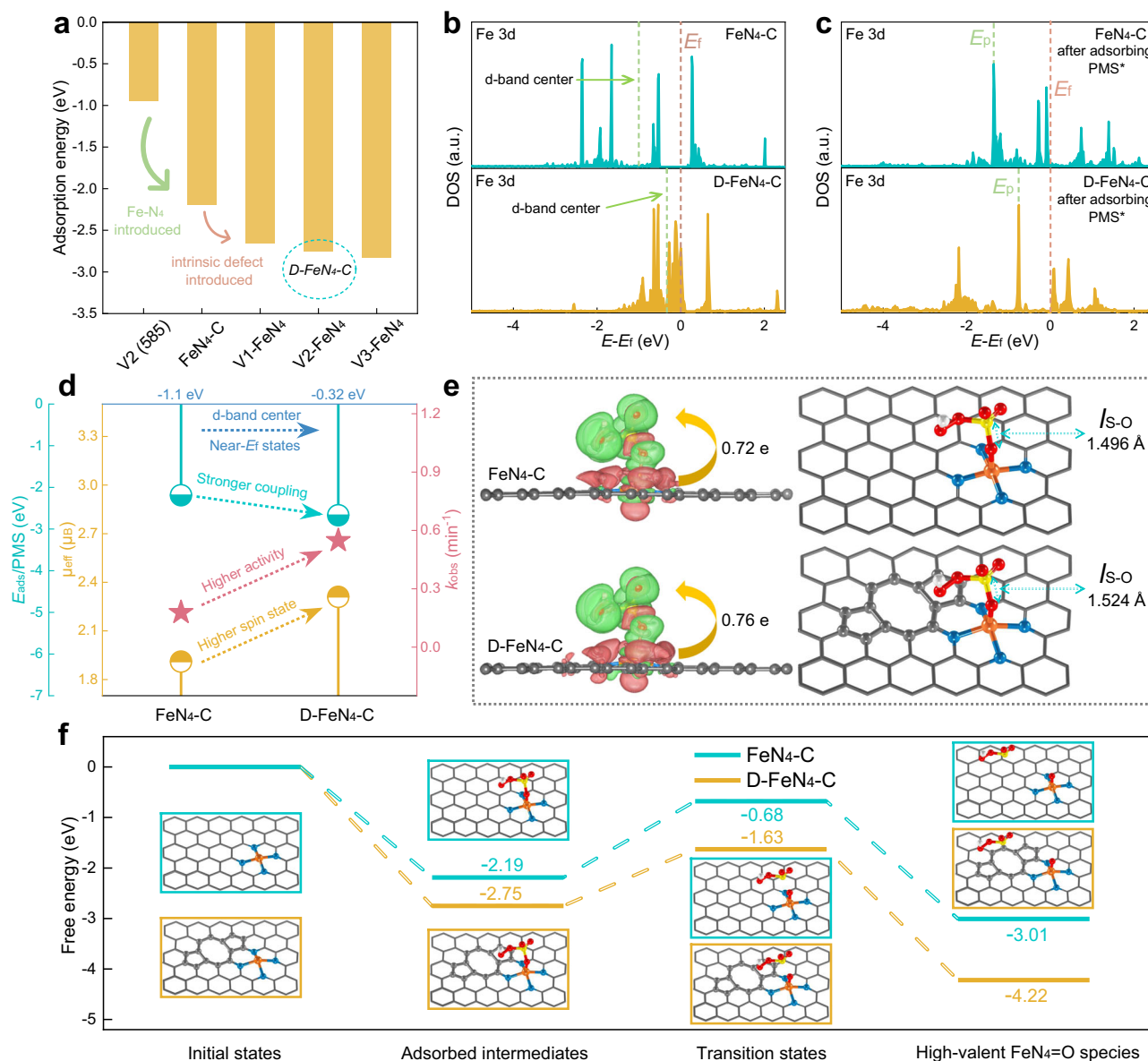
Fig. 4 | Electronic structures and reaction pathways of FeN$_4$−C and D−FeN$_4$−C by inducing intrinsic carbon defects. a PMS adsorption energy on different sites. **b** Projected DOS of Fe 3d in FeN$_4$−C and D−FeN$_4$−C, E_f is at 0 eV. **c** Fe 3d projected DOS of FeN$_4$−C and D−FeN$_4$−C after adsorbing PMS, E_f is at 0 eV. **d** Correlation among the oxidation capacity, coupling strength to PMS, d-band structure and the effective magnetic moment (μ_{eff}) of FeN$_4$−C and D−FeN$_4$−C. **e** Charge density (rouge and green represent the dissipation and aggregation of electrons, respectively) and the S−O bond length (l_{S-O}) in PMS adsorption configurations on FeN$_4$−C and D−FeN$_4$−C. **f** Reaction pathways and the energy profile diagram of PMS dissociation and FeN$_4$=O generation on FeN$_4$−C and D−FeN$_4$−C (inset: corresponding intermediate structures). Source data are provided as a Source Data file.

−0.95 eV) are much inferior to Fe−N$_4$ sites (−2.83 eV to −2.19 eV), indicating the weak coupling to PMS and matching the experimental results (Fig. 4a, Supplementary Figs. 39, 40). Compared with FeN$_4$−C, the doped-585-defect site in D−FeN$_4$−C modifies the electronic structure of graphene, releasing more free electrons and accumulating into the Fe−N$_4$ site to form electron-rich regions (Supplementary Fig. 41). Neighboring defects induced alterations in Fe−N bond lengths and charge redistribution of Fe−N$_4$ sites, disrupting the original symmetric charge state (Supplementary Figs. 42, 43). High electron density facilitates catalyzing the adsorbed PMS and modulating the reactivity of reaction intermediates.

The long-range interactions of the 585 defects on the neighboring Fe−N$_4$ sites remarkably narrow the d-band of Fe atoms in calculated density of electronic states (DOS), and the optimized electron distribution of the Fe atom elevates the d-band center from −1.11 eV for FeN$_4$−C to −0.32 eV for D−FeN$_4$−C (Fig. 4b). Following the Newns-Anderson-Grimley theory, the more centralized d orbitals tend to split to create bonding and antibonding orbitals when interacting with the adsorbate under energy level matching to firmer adsorption[43]. Furthermore, the disparity in Fe 3d DOS for FeN$_4$−C and D−FeN$_4$−C after PMS adsorption was also investigated. The adsorption strength of the intermediates can be inferred from the position of the highest electronic peak states (E_p). As illustrated in Fig. 4c, the energy level position of E_p after PMS adsorption by D−FeN$_4$−C is closer to the Fermi level (E_f), which implies that the lower filling of the antibonding state and responds to stronger bonding to adsorbates[44]. To further elucidate the regulation of the spin states at Fe centers by intrinsic defects, we calculated the effective magnetic moments (μ_{eff}) based on the χ^{-1}−T

curves (Supplementary Fig. 44)[45]. Larger magnetic moments of D−FeN$_4$−C (μ_{eff} = 2.31 μ_B, and μ_B is Bohr magneton) than FeN$_4$−C (μ_{eff} = 1.94 μ_B) suggest that the intrinsic defect-modified D−FeN$_4$−C possesses higher spin states. Meanwhile, consistent with experimental μ_{eff} values, the possible theoretical μ_{eff} values equally found the higher spin state of the Fe species in D−FeN$_4$−C under the identical Fe spin numbers (Supplementary Table 6). The introduction of intrinsic defects still increased unpaired electron numbers, accompanied by enhancement of the electron density of the Fe−N$_4$ sites, even though the Fe in both FeN$_4$−C and D−FeN$_4$−C retained high spin states (from Mössbauer spectroscopy analysis)[46]. Combined with the positive correlation among spin state, E_{ads} and the oxidation capacities (Fig. 4d), incorporation defects induced the near-Fermi electronic states and high-spin states of Fe−N$_4$ sites and decreases in orbital occupancy, thus boosting the bonding strength and reaction kinetics.

Electrochemical impedance spectroscopy (EIS) tests show that D−FeN$_4$−C carrying intrinsic defects possesses less internal charge transfer resistance than FeN$_4$−C (Supplementary Fig. 45)[25]. Meanwhile, stronger coupling and accelerated charge transfer between the Fe−N$_4$ sites and PMS extended the S−O bond length, contributing to the generation of FeN$_4$=O (Fig. 4e and Supplementary Fig. 46). The modification of neighboring intrinsic carbon defects on the free energy of the FeN$_4$=O generation was further calculated (Fig. 4f). Firstly, the Fe−N$_4$ site adsorbs the PMS molecule and releases energy. Then, the adsorbed PMS is activated, and the S−O bond undergoes stretching and breakage. Subsequently, HSO$_4^-$ desorption forms FeN$_4$=O intermediates. Inspiringly, upon modification with intrinsic defects, the transition state (TS) involved in the critical step of S−O bond cleavage to form FeN$_4$=O is thermodynamically more favorable, and the energy barrier to be overcome is lowered by 0.39 eV, indicating the much higher conversion potential to form high-valent FeN$_4$=O in D−FeN$_4$−C. The total energy released by D−FeN$_4$−C/PMS during reactions is 4.22 eV, which is higher than that of FeN$_4$−C/PMS (3.01 eV). Previous literature has reported that high-spin Fe^{III}−N$_4$ species were thermodynamically and kinetically favorable for generating high-valent FeN$_4$=O species upon binding to PMS[47]. Combined with Mössbauer spectroscopy analysis, the high spin state and high concentrations of high-spin Fe^{III}−N$_4$ species in D−FeN$_4$−C resulted in relatively low formation energy of high-valent FeN$_4$=O, thus accelerating the electron transfer from the organic pollutant molecules to the Fe−O π* orbitals[47]. However, the coupling of the defects to the Fe−N$_4$ sites cannot thermodynamically enhance $^1O_2$ generation, which is consistent with the mechanism analysis results (Supplementary Fig. 47). All these calculations essentially signify that intrinsic defect could regulate electronic structures of neighboring Fe−N$_4$ sites and enhance intrinsic reactivity by strengthening charge transfer and reducing the reaction barrier to realizing highly efficient pollutant degradation.

Sustainability assessment and environmental applications

Life cycle assessment (LCA) was initiated to quantify the sustainability and environmental impacts of the D−FeN$_4$−C/PMS process[48]. Concurrently, we adopted the Fe-based PMS catalytic systems constructed from the extensively reported Fe SACs derived from zeolitic imidazolate frameworks (ZIF-derived FeSA) and the conventional Fe$_3$O$_4$ catalysts as comparisons[49,50]. Specifically, we considered the entire water treatment process, including both catalyst preparation and pollutant degradation, with 18 relevant descriptors, and all data are at the lab scale (Supplementary Fig. 48 and Supplementary Tables 7, 8). As shown in Fig. 5a, it is apparent that the preparation process of Fe$_3$O$_4$ presents much lower environmental impacts than SACs for most descriptors, which is attributed to the more complicated synthesis conditions of SACs. As expected, the preparation of D−FeN$_4$−C possesses evident superiority over ZIF-derived FeSA, indicating that the synthesis of D−FeN$_4$−C in this work is more cost-effective and eco-friendly. Considering that the equipment can be operated under full

load conditions and resources can be maximized when industrial production scale is achieved in the future, the environmental impact of SACs at the preparation stage will be highly reduced. It is noteworthy that the high-performance SACs provide distinct advantages versus Fe$_3$O$_4$ in the pollutant degradation stage. The D−FeN$_4$−C system also has a lower environmental impact than the ZIF-derived FeSA in treating SIZ wastewater, owing to the less catalyst/PMS requirement and electricity consumption stemming from the higher intrinsic activity of D−FeN$_4$−C. Lower raw material consumption also implies reduced transport costs from the place of production to the wastewater treatment plant in real-world applications, further reducing the environmental impact.

The excellent properties of D−FeN$_4$−C inspire us to further extend the potential for practical applications at the device level. Two continuous-flow microreactors with different sizes were employed to evaluate the long-term stability by continuously treating the simulated and actual wastewater (Fig. 5b and Supplementary Figs. 49, 50). Catalysts were homogeneously fixed by cotton in the microreactor, while the enlarged microreactor was filled with catalysts-loaded polyurethane (PU) sponges. The microreactor system loaded with D−FeN$_4$−C could totally remediate 6 L SIZ wastewater without cleaning at the flow rate of 2 mL min^{-1}, but degradation rates gradually decreased at the terminal under the high flow rate of 5 mL min^{-1}, indicating the overloading of pollutants (Fig. 5c). Conversely, FeN$_4$−C showed inferior stability, with a significant decline in SIZ degradation under high flow rate conditions. In addition, D−FeN$_4$−C also exhibited improved performance over FeN$_4$−C in TOC removal for actual hospital wastewater (Fig. 5d). However, even at the low flow rate of 1 mL min^{-1}, the D−FeN$_4$−C system only achieved nearly 50% TOC removal after recollecting and re-pumping primary-treated effluent, indicating that the limited volume and catalyst loading of the microreactor cannot respond to higher-intensity pollutant loadings.

The enlarged microreactor was designed to broaden the practical application potential (see Supplementary Fig. 51 with accompanying detailed discussion for the characterization of catalysts-loaded PU sponges). SIZ removal in the device equipped with D−FeN$_4$−C-loaded PU sponges was consistently maintained at 100% at high pumping speeds of 10 mL min^{-1} and even 20 mL min^{-1} in treating 60 L SIZ wastewater (Fig. 5e), demonstrating excellent catalytic capacity and stability of the scale-up reaction device. The D−FeN$_4$−C-loaded PU sponges were also resistant to shock loading and remained uniformly distributed without significant loss in reactions attributed to the strong bonding strength. (Supplementary Fig. 52). Notably, upon application of the enlarged microreactor for actual hospital wastewater treatment, the D−FeN$_4$−C/PMS system achieved high TOC removal after repeated operations. As shown in Fig. 5f and Supplementary Table 9, 72.2%–83.5% TOC removal and 67.1%–76.9% COD removal were achieved after continuous treatment, and the final effluent met the discharge standard for medical organizations in China (GB18466-2005) (Supplementary Fig. 53). Accordingly, the Fe leaching concentration during reaction systems was under 100 μg L^{-1} without severe secondary contamination, far below the limit of 300 μg L^{-1} in standards for drinking water quality in China (GB 5749-2022). Thus, the processing capacity of the catalytic systems can be scaled up simultaneously by expanding reactor capacity and catalyst loading, demonstrating the enormous potential for practical hospital wastewater treatment (Fig. 5g). Overall, the wastewater treatment process constructed by intrinsic carbon defects-modified D−FeN$_4$−C and PMS offers a green and sustainable approach to sustainable water purification.

Discussion
In this study, intrinsic topological defects were successfully created in two-dimensional carbon planes loaded with Fe−N$_4$ sites via an
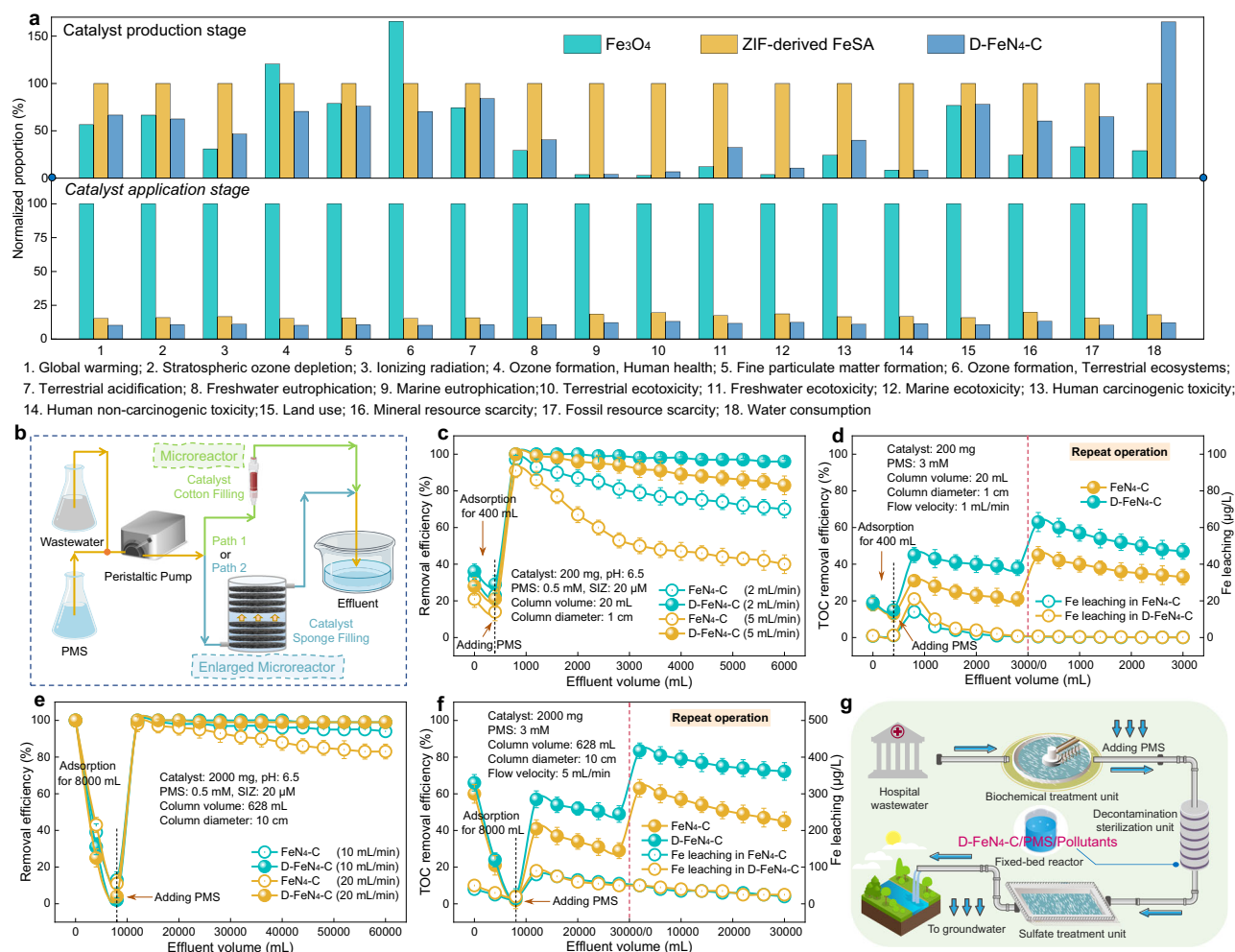
Fig. 5 | Life cycle assessment (LCA) and potential in actual sewage treatment. a Relative environmental impact of environmentally relevant descriptors for treating 1 kg SIZ in Fenton-like processes with Fe_3O_4/PMS, ZIF-derived FeSA/PMS and D−FeN₄−C/PMS systems. **b** Schematic diagram of the continuous-flow catalytic unit coupled with microreactor or enlarged microreactor. **c, d** Treatment of SIZ and actual hospital wastewater by the microreactor and the Fe leaching concentration.

e, f Treatment of SIZ and actual hospital wastewater by the enlarged microreactor and the Fe leaching concentration. **g** Schematic illustration for the possible industrial hospital wastewater treatment with D−FeN₄−C as the heterogeneous Fenton-like catalyst. Reaction condition for **d** and **f**: [TOC of hospital wastewater] = 49.70 mg L⁻¹. Error bars are standard error values of three tests (n = 3). Source data are provided as a Source Data file.

elaborate strategy of N species elimination. Integration of neighboring intrinsic carbon defects with Fe−N₄ moieties significantly elevated the intrinsic reactivity and stability of Fe−N₄ sites and boosted the PMS activation performance of D−FeN₄−C for SIZ degradation. Mechanistic investigations revealed that introducing intrinsic carbon defects enhanced FeN₄=O generation without influencing ¹O₂ production. DFT calculations confirmed that the constructed 585 defects strengthened the coupling of neighboring Fe−N₄ sites with PMS and reduced reaction barriers for producing FeN₄=O species by optimizing the Fe 3d orbitals through long-range interactions. Further life cycle assessment and device-level operation suggested that the D−FeN₄−C-based reactor system achieved long-term stability with strong environmental viability during continuous simulated and actual wastewater treatment. These findings open a new avenue for developing highly efficient and durable SAC for sustainable water decontamination.

Methods

Synthetic strategy of Fe SACs

Under room temperature, 16 g DCD and 2 g CEPI were dissolved in 400 mL methanol. After stirring for 10 h, elevate the temperature to 80 °C to remove methanol by evaporation. The obtained solid was

thoroughly ground and put into a crucible with a lid, then heated in a muffle furnace at 550 °C for 4 h with a heating rate of 2.5 °C min⁻¹ to obtain CEPI-modified g-C₃N₄. The synthesis procedure of Fe-g-C₃N₄ was identical to that of g-C₃N₄ except for adding 24 mg or 15 mg Fe(NO₃)₃•9H₂O in the raw materials. Fe-g-C₃N₄ was carbonized at 800 °C (with 24 mg Fe(NO₃)₃•9H₂O added) and 900 °C (with 15 mg Fe(NO₃)₃•9H₂O added) for 2 h, with a heating rate of 5 °C min⁻¹ under N₂ atmosphere, to obtain FeN₄−C and D−FeN₄−C, respectively. Under the same conditions, NC and DNC were prepared as reference samples by pyrolyzing CEPI-modified g-C₃N₄ at 800 °C or 900 °C. Fe_{NP}−NC was obtained by calcining the precursors of D−FeN₄−C at 1000 °C. D−FeN₄−C was regenerated by pyrolysis at 900 °C for 1 h.

Catalytic activity evaluation for Fenton-like reaction

The degradation tests were conducted in a 250 mL reactor, and the reaction volume was 100 mL. Typically, 5 mg catalyst was dispersed into the SIZ solution. The reaction was triggered after adding PMS. 1 mL of liquid was withdrawn and quenched with 30 μL Na₂S₂O₃ solution at each time interval, and the residual SIZ was measured using HPLC. All experiments are conducted at 25 °C. In the recycling test, the catalyst was collected after each run, fully washed with adequate

amounts of ethanol and Milli-Q water, and dried before the next recycling. All experiments were conducted in duplicate or triplicate to ensure reproducibility.

Characterizations

Fe K-edge XAS analyzes were performed with Si(111) crystal monochromators at the BL14W Beamline at the Shanghai Synchrotron Radiation Facility (SSRF) (Shanghai, China). Samples were compressed into pellets, and the XAFS spectra were collected at the transmission mode. EXAFS data analysis was performed using the ATHENA and ARTEMIS programs in the Demeter computer package[51]. Concentrations of contaminants were analyzed by HPLC (Agilent, USA) equipped with a UV detector and an Eclipse XDB C18 (5 µm, 4.6 × 250 mm) (Supplementary Table 10). The Raman measurements were carried out on a Raman Spectrometer (HORIBA-800) with a 514 nm laser as the excitation source. Element content analysis was performed on an inductively coupled plasma mass spectrometer (ICP-OES730, Agilent). The atomic-resolution HAADF-STEM imaging and EDS and EELS analysis were performed on an FEI Titan Themis apparatus with an X-FEG electron gun and a DCOR aberration corrector operating at 300 kV. Atomic force microscopy (AFM) images were performed by an AFM microscope XE-100E in the air condition. Total organic carbon (TOC) analyzes were realized by TOC analyzer (Shimadzu TOC-L CPH). Chemical oxygen demand (COD) was measured by a COD rapid tester (5B-3C(V8), Lianhua Technology). The ammonia concentration (NH_3-N) was measured by the HI-96715 ammonia analyzer (Hanna, Italy). Molybdenum antimony anti-spectrophotometry was used to determine total phosphorus (TP). BET-specific surface areas and pore size distribution of the catalysts were ascertained using a Micromeritics ASAP2020 Plus 2.00 system for N_2 adsorption-desorption measurements. Electrochemical measurements were performed on a PARSTAT 4000 A potentiostat workstation (Princeton Applied Research) with a conventional three-electrode cell system. EPR spectra were obtained on Bruker EMX plus X-band CW EPR spectrometer (microwave frequency, 9.83 GHz; microwave power, 2.00 MW). Three-dimensional fluorescence spectroscopy (3DEEMs) was carried out using a fluorescence spectrophotometer (F-7000 FL Spectrophotometer, Hitachi, Japan). Zeta potentials of samples were measured by the Malvern Zetasizer Nano ZS90. Zero field cooled (ZFC) and field cooled (FC) measurements were executed by magnetic property measurement system (MPMS-3, Quantum Design) under H = 500 Oe for temperature-dependent (2–400 K) magnetization measurement. The ^{57}Fe Mössbauer spectra of the samples were measured on a Topologic 500 A spectrometer using a ^{57}Co:Rh source at 298 K and were calibrated with the α-iron foil at 298 K. The recorded Fe Mössbauer spectra were analyzed with the least-square methods.

Theoretical calculation

All DFT calculations were performed by the Vienna ab initio simulation package (VASP v5.4.1)[52,53]. The exchange-correlation interactions were described by using the Perdew-Burke-Ernzerhof in the generalized gradient approximation (GGA-PBE)[54]. The cut-off energy of plane wave was set at 400 eV for valence electrons[55]. The maximum Hellmann-Feynman force for each ionic optimization step is 0.01 eV/Å, and the convergence energy threshold of self-consistent calculations is 10^{-5} eV. The accuracy of geometry optimization converged to 0.02 eVÅ^{-1} and 10^{-5} eV. To ensure the accuracy of the calculation results on the simulated crystal surface, the vacuum layer was set as 20 Å. The Gaussian smearing width was set to 0.05 eV. Van der Waals interactions were accounted for via the zero damping DFT-D3 method. Due to the magnetism of transition metal elements, spin polarization was considered in all calculations[56]. We established initial magnetic moments for Fe atom based on the possible valence states and conducted single-point energy calculations.

Data availability

The authors declare that all the data supporting the findings of this study are available within the article and the Supplementary Information file. Source data are also provided as a Source Data file. Source data are provided with this paper.

References

1. Liu, T. et al. Water decontamination via nonradical process by nanoconfined Fenton-like catalysts. *Nat. Commun.* **14**, 2881 (2023).
2. Yu, F. et al. Rapid self-heating synthesis of Fe-based nanomaterial catalyst for advanced oxidation. *Nat. Commun.* **14**, 4975 (2023).
3. Bao, Y. et al. Generating high-valent iron-oxo identical with Fe(IV)=O complexes in neutral microenvironments through peroxymonosulfate activation by zn-fe layered double hydroxides. *Angew. Chem. Int. Ed.* **61**, e202209542 (2022).
4. Chen, Z. et al. Single-atom Mo-Co catalyst with low biotoxicity for sustainable degradation of high-ionization-potential organic pollutants. *Proc. Natl Acad. Sci. USA* **120**, e2305933120 (2023).
5. Zhou, X. et al. Identification of Fenton-like active Cu sites by heteroatom modulation of electronic density. *Proc. Natl Acad. Sci. USA* **119**, e2119492119 (2022).
6. Zhou, Q. et al. Generating dual-active species by triple-atom sites through peroxymonosulfate activation for treating micropollutants in complex water. *Proc. Natl Acad. Sci. USA* **120**, e2300085120 (2023).
7. Mo, F. et al. The optimized Fenton-like activity of Fe single-atom sites by Fe atomic clusters-mediated electronic configuration modulation. *Proc. Natl Acad. Sci. USA* **120**, e2300281120 (2023).
8. Song, J. et al. Asymmetrically coordinated cob1n3 moieties for selective generation of high-valence co-oxo species via coupled electron-proton transfer in fenton-like reactions. *Adv. Mater.* **35**, e2209552 (2023).
9. Gu, C.-H. et al. Slow-release synthesis of Cu single-atom catalysts with the optimized geometric structure and density of state distribution for Fenton-like catalysis. *Proc. Natl Acad. Sci. USA* **120**, e2311585120 (2023).
10. Jiang, X. et al. Precise coordination of high-loading Fe single atoms with sulfur boosts selective generation of nonradicals. *Proc. Natl Acad. Sci. USA* **121**, e2309102121 (2024).
11. Yu, X. et al. A green edge-hosted zinc single-site heterogeneous catalyst for superior Fenton-like activity. *Proc. Natl Acad. Sci. USA* **120**, e2221228120 (2023).
12. Jiang, Y. et al. In situ turning defects of exfoliated Ti_3C_2 MXene into Fenton-like catalytic active sites. *Proc. Natl Acad. Sci. USA* **120**, e2210211120 (2023).
13. Qu, W. et al. Accelerated catalytic ozonation in a mesoporous carbon-supported atomic fe-n4 sites nanoreactor: confinement effect and resistance to poisoning. *Environ. Sci. Technol.* **57**, 13205–13216 (2023).
14. Chen, F. et al. Single-atom iron anchored tubular g-c3n4 catalysts for ultrafast fenton-like reaction: roles of high-valency iron-oxo species and organic radicals. *Adv. Mater.* **34**, e2202891 (2022).
15. Liang, X. et al. Coordination number dependent catalytic activity of single-atom cobalt catalysts for fenton-like reaction. *Adv. Funct. Mater.* **32**, 2203001 (2022).
16. Zhao, Z. et al. Enhanced interfacial electron transfer by asymmetric cu-ov-in sites on in2o3 for efficient peroxymonosulfate activation. *Angew. Chem. Int. Ed.* **62**, e202216403 (2023).
17. Huang, B. et al. Modulating electronic structure engineering of atomically dispersed cobalt catalyst in fenton-like reaction for efficient degradation of organic pollutants. *Environ. Sci. Technol.* **57**, 14071–14081 (2023).
18. Ling, L. L. et al. Potassium-assisted fabrication of intrinsic defects in porous carbons for electrocatalytic co2 reduction. *Adv. Mater.* **34**, e2205933 (2022).

19. Cheng, Q. et al. Carbon-defect-driven electroless deposition of pt atomic clusters for highly efficient hydrogen evolution. *J. Am. Chem. Soc.* **142**, 5594–5601 (2020).

20. Wang, X. et al. A directional synthesis for topological defect in carbon. *Chem* **6**, 2009–2023 (2020).

21. Kong, Y. et al. Accelerating protonation kinetics for ammonia electrosynthesis on single iron sites embedded in carbon with intrinsic defects. *Adv. Funct. Mater.* **32**, 2205409 (2022).

22. Wei, S. et al. Self-carbon-thermal-reduction strategy for boosting the Fenton-like activity of single $Fe-N_4$ sites by carbon-defect engineering. *Nat. Commun.* **14**, 7549 (2023).

23. Ni, W. et al. Electroreduction of carbon dioxide driven by the intrinsic defects in the carbon plane of a single $fe-N_4$ Site. *Adv. Mater.* **33**, e2003238 (2021).

24. Tian, H. et al. High durability of Fe-N-C single-atom catalysts with carbon vacancies toward the oxygen reduction reaction in alkaline media. *Adv. Mater.* **35**, e2210714 (2023).

25. Guo, R. et al. Effect of intrinsic defects of carbon materials on the sodium storage performance. *Adv. Energy Mater.* **10**, 1903652 (2020).

26. Dong, Y. et al. Ammonia thermal treatment toward topological defects in porous carbon for enhanced carbon dioxide electro-reduction. *Adv. Mater.* **32**, e2001300 (2020).

27. Guan, L. et al. Intrinsic defect-rich hierarchically porous carbon architectures enabling enhanced capture and catalytic conversion of polysulfides. *ACS Nano* **14**, 6222–6231 (2020).

28. Li, Z. et al. Regulating the N coordination environment of Co single-atom nanozymes for highly efficient oxidase mimics. *Nano Lett.* **23**, 1505–1513 (2023).

29. Liang, J. et al. Regulating the coordination environment of mesopore-confined single atoms from metalloprotein-MOFs for highly efficient biocatalysis. *Adv. Mater.* **34**, e2205674 (2022).

30. Wang, W. et al. Intrinsic carbon-defect-driven electrocatalytic reduction of carbon dioxide. *Adv. Mater.* **31**, e1808276 (2019).

31. Wang, F. et al. Intrinsic carbon defects induced reversible antimony chemistry for high-energy aqueous alkaline batteries. *Adv. Mater.* **34**, e2200085 (2022).

32. Zhong, L. et al. ^{57}Fe-Mössbauer spectroscopy and electrochemical activities of graphitic layer encapsulated iron electrocatalysts for the oxygen reduction reaction. *Appl. Catal. B: Environ.* **221**, 406–412 (2018).

33. Zeng, Y. et al. Unraveling the electronic structure and dynamics of the atomically dispersed iron sites in electrochemical CO_2 reduction. *J. Am. Chem. Soc.* **145**, 15600–15610 (2023).

34. Yang, M. et al. Unveiling the origins of selective oxidation in single-atom catalysis via $Co-N_4$-C intensified radical and nonradical pathways. *Environ. Sci. Technol.* **56**, 11635–11645 (2022).

35. Li, X. et al. CoN_1O_2 single-atom catalyst for efficient peroxymonosulfate activation and selective cobalt(iv)=o generation. *Angew. Chem. Int. Ed.* **62**, e202303267 (2023).

36. Ren, W. et al. Origins of electron-transfer regime in persulfate-based nonradical oxidation processes. *Environ. Sci. Technol.* **56**, 78–97 (2022).

37. Cheng, C. et al. Generation of Fe(IV)=O and its contribution to fenton-like reactions on a single-atom iron-N-C catalyst. *Angew. Chem. Int. Ed.* **62**, e202218510 (2023).

38. Zhou, H. et al. High-valent metal-oxo species transformation and regulation by co-existing chloride: Reaction pathways and impacts on the generation of chlorinated by-products. *Water Res* **257**, 121715 (2024).

39. Zhang, H. C. et al. Axial N ligand-modulated Ultrahigh Activity And Selectivity Hyperoxide Activation Over Single-atoms Nanozymes. *Adv. Sci.* **10**, e2205681 (2023).

40. Yu, X. et al. Coupling of iron phthalocyanine at carbon defect site via π-π stacking for enhanced oxygen reduction reaction. *Appl. Catal. B: Environ.* **280**, 119437 (2021).

41. Yang, S. et al. Overlooked role of nitrogen dopant in carbon catalysts for peroxymonosulfate activation: Intrinsic defects or extrinsic defects? *Appl. Catal. B: Environ.* **295**, 120291 (2021).

42. Ren, W. et al. Insights into the electron-transfer regime of peroxydisulfate activation on carbon nanotubes: the role of oxygen functional groups. *Environ. Sci. Technol.* **54**, 1267–1275 (2019).

43. Greiner, M. T. et al. Free-atom-like d states in single-atom alloy catalysts. *Nat. Chem.* **10**, 1008–1015 (2018).

44. Chen, Z. et al. Amination strategy to boost the CO_2 electroreduction current density of M–N/C single-atom catalysts to the industrial application level. *Energy Environ. Sci.* **14**, 2349–2356 (2021).

45. Song, J. et al. Unsaturated single-atom CoN_3 sites for improved fenton-like reaction towards high-valent metal species. *Appl. Catal. B: Environ.* **325**, 122368 (2023).

46. Chai, Y. et al. Elucidation of the mechanistic origin of spin-state-dependent P-doped Fe single-atom catalysts for the oxidation of organic pollutants through peroxymonosulfate activation. *Appl. Catal. B: Environ.* **341**, 123289 (2024).

47. Zhang, B., Li, X., Akiyama, K., Bingham, P. A. & Kubuki, S. Elucidating the mechanistic origin of a spin state-dependent fenx-c catalyst toward organic contaminant oxidation via peroxymonosulfate activation. *Environ. Sci. Technol.* **56**, 1321–1330 (2022).

48. Liu, X.-C. et al. Tuning Fe_3O_4 for sustainable cathodic hetero-geneous electro-Fenton catalysis by acetylated chitosan. *Proc. Natl Acad. Sci. USA* **120**, e2213480120 (2023).

49. Wu, Z. et al. Facilely tuning the first-shell coordination micro-environment in iron single-atom for fenton-like chemistry toward highly efficient wastewater purification. *Environ. Sci. Technol.* **57**, 14046–14057 (2023).

50. Yang, Q. et al. Heterogeneous activation of peroxymonosulfate by different ferromanganese oxides for tetracycline degradation: Structure dependence and catalytic mechanism. *Chem. Eng. J.* **348**, 263–270 (2018).

51. Ravel, B. & Newville, M. ATHENA, ARTEMIS, HEPHAESTUS: data analysis for X-ray absorption spectroscopy using IFEFFIT. *J. Synchrotron Radiat.* **12**, 537–541 (2005).

52. Kresse, G. & Furthmüller, J. Efficiency of ab-initio total energy calculations for metals and semiconductors using a plane-wave basis set. *Comput. Mater. Sci.* **6**, 15–50 (1996).

53. Blöchl, P. E. Projector augmented-wave method. *Phys. Rev. B* **50**, 17953–17979 (1994).

54. Perdew, J. P. et al. Atoms, molecules, solids, and surfaces: Applications of the generalized gradient approximation for exchange and correlation. *Phys. Rev. B* **46**, 6671–6687 (1992).

55. Mathew, K., Sundararaman, R., Letchworth-Weaver, K., Arias, T. A. & Hennig, R. G. Implicit solvation model for density-functional study of nanocrystal surfaces and reaction pathways. *J. Chem. Phys.* **140**, 084106 (2014).

56. Mathew, K., Kolluru, V. S. C., Mula, S., Steinmann, S. N. & Hennig, R. G. Implicit self-consistent electrolyte model in plane-wave density-functional theory. *J. Chem. Phys.* **151**, 234101 (2019).

Acknowledgements

Author contributions

Competing interests

The authors declare no competing interests.

Additional information

Supplementary information The online version contains supplementary material available at https://doi.org/10.1038/s41467-024-52074-2.

Correspondence and requests for materials should be addressed to Sihui Zhan or Bo Lai.

Peer review information *Nature Communications* thanks Derek Hao, Macarena Munoz and the other, anonymous, reviewers for their contribution to the peer review of this work. A peer review file is available.

Reprints and permissions information is available at http://www.nature.com/reprints

Publisher's note Springer Nature remains neutral with regard to jurisdictional claims in published maps and institutional affiliations.